


Numerical analysis of electrohydrodynamic instability in dielectric-liquid–gas flows subjected to unipolar injection

Qiang Liu ¹, Alberto T. Pérez ², R. Deepak Selvakumar,¹ Pengfei Yang,¹ and Jian Wu ^{1,*}

¹Key Laboratory of Aerospace Thermophysics, School of Energy Science and Engineering, Harbin Institute of Technology, Harbin 150001, People's Republic of China

²Departamento de Electrónica y Electromagnetismo, Facultad de Física, Universidad de Sevilla, Avda. de Reina Mercedes s/n, 41013 Sevilla, Spain

 (Received 16 July 2021; revised 4 November 2021; accepted 30 November 2021; published 20 December 2021)

In this work, the electrohydrodynamic instability induced by a unipolar charge injection is extended from a single-phase dielectric liquid to a two-phase system that consists of a liquid-air interface. A volume-of-fluid model-based two-phase solver was developed with simplified Maxwell equations implemented in the open-source platform OpenFOAM. The numerically obtained critical value for the linear stability matches well with the theoretical values. To highlight the effect of the slip boundary at interface, the deformation of the interface is ignored. A bifurcation diagram with hysteresis loop linking the linear and finite-amplitude criteria, which is $U_f = 0.059$, was obtained in this situation. It is concluded that the lack of viscous effect at interface leads to a significant increase in the flow intensity, which is the reason for the smaller instability threshold in two-phase system. The presence of interface also changes the flow structure and results in a shear distribution of electric force, which may play an important role in the interface deformation.

DOI: [10.1103/PhysRevE.104.065109](https://doi.org/10.1103/PhysRevE.104.065109)

I. INTRODUCTION

Multiphase electrohydrodynamics (EHD) is a complex subject that involves interactions of two or more fluids and also an external electric field. It attracts a wide range of fundamental research interest due to its complex flow structures and rich bifurcations [1–5]. This type of flow motion also plays the center role in several engineering applications, such as electrospays, ink-jets, boiling heat transfer, and EHD pumping [6–10]. Besides, several research on the so-called EHD mixers, which use electric field to mix two incompatible liquids between plate electrodes, has been reported [11–13]. These studies involve a kind of classical problem: stability of the interface under the electric field.

In a two-phase EHD problem, the stability of the interface between two fluid layers was first discussed by Taylor and McEwan [14]. They gave a theoretical and experimental analysis to the instability of a perfect conducting liquid layer placed between two plane electrodes. A flourish of extending this topic from various aspects has occurred in recent years. For example, it has been proved that the electric field is able to produce many different flow patterns in the absence of shear flow between layers [15–17]. Some typical interface instabilities between two fluid layers like the Rayleigh-Taylor instability can also be controlled by electric field [18–20]. When the shear flow is considered, the problem turns into film flow under the electric field and the original instability will be affected significantly due to the enriched interplay among the electric force, viscous stress, and surface tension [21–24]. The

influence of the wall topography [25–27] as well as the ac-dc characteristics of the electric field [28–30] on film stability are also widely studied.

Inspired by the experimental observation of Rose window instability [31,32], the gas-liquid flow subjected to charge injection has also attracted many research interests. The Rose window instability arises when a corona discharge is applied on a liquid surface with low conductivity. The electric field pushes the charged liquid surface and a regular interface deformation like a Rose window appears. Intrigued by the flow pattern of Rose window instability, Atten and Koulova-Nenova gave a linear stability analysis with a two-dimensional (2D) model considering a layer of liquid and a layer of air between parallel plates under unipolar injection [33,34]. No criterion related to Rose window instability was found in their work but a criterion for the EHD instability caused by bulk charge in liquid layer is obtained. The EHD instability caused by bulk charge is a classical research topic in electrohydrodynamics [35,36]. The injected charge in the liquid bulk tends to destabilize the system and trigger the flow motion. The hydrostatic state will be broken when the driving parameter is higher than creation obtained by linear stability analysis [37]. Besides, research also predicts a subcritical bifurcation and a nonlinear finite-amplitude criterion which is induced by the electric migration of the charge carriers with a finite ionic velocity under electric field [38]. Since the finite-amplitude criterion is lower than the linear one, a hysteresis loop is established and this hysteresis characteristic can be reflected by measuring the voltage current curve of the system in the experiments [39]. The competition between electric migration and flow convection in the transportation of free charge leads to the formation of the so-called charge void region. The

*jian.wu@hit.edu.cn

charge void region refers to an area with very thin charge density where the electric migration of charge is offset by the convection [35,36,40]. In the charge void region, inner charge is transported out of the area due to the dominate convection and external charge cannot be injected into the region with the neutralized electric migration. The existence of hysteresis loop and charge void region has been proved by experiments [39,41] and numerical simulations [42–44], and these two phenomena are considered as the key features of the EHD instability induced by the charge in the liquid bulk. Atten and Koulova-Nenova's work showed that the deformation of the interface will decrease the linear critical value for the bulk charge instability compared to a single-phase dielectric fluid system. Many subsequent works tried to find the critical value corresponding to the Rose window instability [45–47] based on Atten and Koulova-Nenova's work and this was finally made by Chicón and Pérez [48]. The bulk charge instability threshold they found is close to Koulova-Nenova's value and a new criterion which is related to the Rose window instability was obtained when the thickness of liquid layer is small enough.

In the configuration of Rose window instability system, the interface works as a flexible electrode from the perspective of liquid layer. This flexible electrode has two key differences compared with the rigid one in single-phase situation, which are the deformability and the slip boundary condition. The effect of deformability is discussed by Koulova-Nenova and Atten as mentioned before while the role of slip boundary has not been carefully studied. Based on the previous numerical studies on the single-phase EHD instability problem [42–44] and the latest analytical work [48], this work presents a numerical analysis of EHD instability of a horizontal liquid-air interface subjected to unipolar charge injection with specifically developed finite-volume solver based on the open-source platform OpenFOAM [49]. The effect of slip boundary condition on the bulk charge instability has been highlighted. The remainder of the paper is organized as follows: A description of the physical problem and the mathematical formulation is presented in the next section; the numerical methodology is described in Sec. III; the results are presented and discussed in Sec. IV; and, finally, the concluding remarks are summarized in the last section.

II. MATHEMATICAL FORMULATION

A. Problem description and governing equations

The flow domain shown in Fig. 1 consists of two flat plate electrodes in parallel configuration that encloses a layer of dielectric liquid and a layer of air with the thicknesses of D and L , respectively. The upper plate electrode is maintained at a higher electric potential $\phi = \phi_0 > 0$ and the bottom electrode is grounded. It is assumed that unipolar injection of positive ions takes place from the upper emitter electrode. A uniform and constant charge density $\rho_e = \rho_{e0}$ (i.e., a homogeneous and autonomous injection) is considered at the emitter electrode.

Both the liquid and air are considered to be incompressible, Newtonian, and perfectly insulating. Following previous theoretical and numerical studies, the governing equations for the

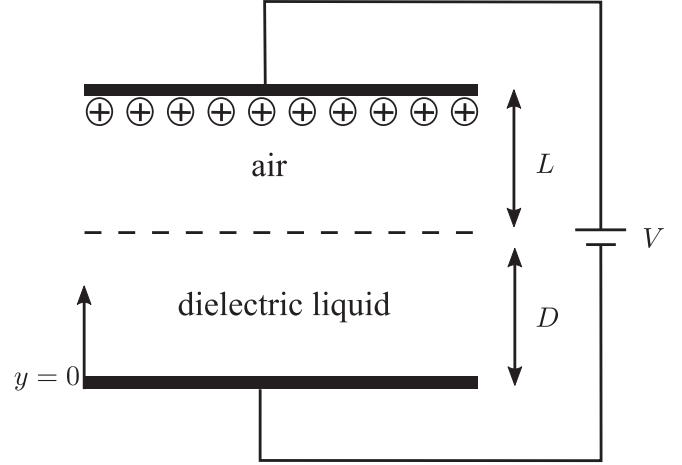


FIG. 1. The schematic diagram of the air-liquid EHD problem.

flow motion consists of classical continuity and momentum equations [48]:

$$\nabla \cdot \mathbf{u} = 0, \quad (1)$$

$$\begin{aligned} \frac{\partial \rho \mathbf{u}}{\partial t} + \nabla \cdot (\rho \mathbf{u} \mathbf{u}) \\ = \nabla \cdot (\mu \nabla \mathbf{u}) - \nabla p + \rho \mathbf{g} + \mathbf{F}_e + \sigma (\nabla_s \cdot \mathbf{n}). \end{aligned} \quad (2)$$

Here $\mathbf{u} = (u_x, u_y)$ is the velocity of the fluid, ρ is the density, μ is the dynamic viscosity, and p is the pressure. The body force $\rho \mathbf{g}$ refers to the gravity pointing to the negative direction of the y axis, and $\sigma (\nabla_s \cdot \mathbf{n})$ is the surface tension force where σ is the surface tension coefficient, ∇_s is the surface gradient operator [1,50], and \mathbf{n} is the unit vector normal to the interface and pointing toward the liquid. The electric force \mathbf{F}_e is calculated from the divergence of Maxwell stress tensor in incompressible fluid [51]:

$$\mathbf{F}_e = \nabla \cdot \left(\varepsilon \mathbf{E} \mathbf{E} - \frac{\varepsilon E^2}{2} \mathbb{I} \right) = \rho_e \mathbf{E} - \frac{1}{2} E^2 \nabla \varepsilon, \quad (3)$$

where ρ_e is the charge density, ε is permittivity, and \mathbb{I} is the unit tensor. The first term and second term in Eq. (3) represent the Coulomb force determined by the charge density and the dielectric force caused by the permittivity differences of two phases, respectively. The electric field \mathbf{E} and charge density ρ_e in Eq. (3) can be obtained by solving the simplified Maxwell equations as follows [48]:

$$\mathbf{E} = -\nabla \phi, \quad (4)$$

$$\nabla \cdot (\varepsilon \nabla \phi) = -\rho_e, \quad (5)$$

$$\frac{\partial \rho_e}{\partial t} + \nabla \cdot (\rho_e \mathbf{u}) + \nabla \cdot (\rho_e K \mathbf{E}) = 0. \quad (6)$$

Here ϕ represented the electric potential, K is the ion mobility and D is the diffusion coefficient. Besides the transient term, the convection, electromigration, and diffusion of charge transportation are expressed from left to right in Eq. (6). In general, the contribution of charge diffusion is very small when compared to convection and electromigration [52].

The liquid and air regions are differentiated by solving a scalar transport equation for the local liquid volume fraction α as follows:

$$\frac{\partial \alpha}{\partial t} + \nabla \cdot (\alpha \mathbf{u}) = 0. \quad (7)$$

The value of α varies from 0 to 1. The regions with $\alpha = 1$ and $\alpha = 0$ are identified as liquid and air, respectively. This interface model is known as the volume-of-fluid (VOF) model [53] and the physical properties are expressed as a function of local liquid fraction as follows:

$$P = \alpha P_l + (1 - \alpha) P_a, \quad (8)$$

where “ P ” represents physical properties including ρ , μ , K , and ε and the subscripts “ l ” and “ a ” indicate the values in the liquid and air regions, respectively.

The boundary conditions at the electrodes have been shown in Fig. 1. The left and right sides of the domain are treated as periodic:

$$u_{x,l} = u_{x,r}, \quad u_{y,l} = u_{y,r}, \quad (9a)$$

$$\phi_l = \phi_r, \quad (9b)$$

$$\rho_{e,l} = \rho_{e,r}, \quad (9c)$$

where the subscripts “ l ” and “ r ” refer to the left boundary and right boundary, respectively. In addition, due to the absence of an interface charge for insulating liquids, the physical quantities satisfy the following relationships at the interface [48]:

$$[\mathbf{E}] \times \mathbf{n} = \mathbf{0}, \quad [\varepsilon \mathbf{E}] \cdot \mathbf{n} = 0, \quad [K \mathbf{E} \rho_e] \cdot \mathbf{n} = 0, \quad (10a)$$

$$\mu \mathbf{t} \cdot (\nabla \mathbf{u} + \nabla \mathbf{u}^T) \cdot \mathbf{n} = 0, \quad (10b)$$

$$- [p] + \mu \mathbf{n} \cdot (\nabla \mathbf{u} + \nabla \mathbf{u}^T) \cdot \mathbf{n} + [\varepsilon (\mathbf{E} \cdot \mathbf{n})^2] - [\frac{1}{2} \varepsilon E^2] - \sigma (\nabla_s \cdot \mathbf{n}) = 0, \quad (10c)$$

where $[A] = A_l - A_a$ represents the jump of any quantity A from liquid to air and \mathbf{t} is the unit vector tangential to interface. Based on Eq. (10a), the ratio of the normal electric fields strength $E_{l,n}/E_{a,n}$ and the ratio of charge density $\rho_{e,l}/\rho_{e,a}$ on the two sides of the interface are equal to $\varepsilon_a/\varepsilon_l$ and $K_a \varepsilon_l/K_l \varepsilon_a$, respectively. Thus, the charge density will have a huge jump at the interface since air usually have smaller permittivity and much larger ion mobility. Equation (10b) and Eq. (10c) give the balance of tangential and normal stress at the interface, respectively. Since the dielectric force only works at the normal direction of the interface and the Coulomb force has no effect to the interface with the absence of interface charge, the right-hand side of Eq. (10b) is zero. Meanwhile, the pressure jump at the interface is determined by the viscous force, dielectric force, and surface tension, as it is showed in Eq. (10c). It is also necessary to point out that the absence of Coulomb force at the interface does not guarantee its absence in the single-phase region near the interface. On the contrary, the role of Coulomb force may become very important considering the jump of charge density at the interface, which will also be highlighted in the following chapters.

B. Nondimensional equations

The above set of governing equations can be rewritten into dimensionless form using the following characteristic scales for length, time, pressure, electric field, charge density,

and electric current density D , $\rho_c D^2/\mu_c$, $\mu_c^2/(\rho_c D^2)$, V/D , $\varepsilon_c V/D^2$, and $\varepsilon_c K_c V^2/D^3$, respectively. Here ρ_c , μ_c , ε_c , and K_c are the characteristic physical properties. The obtained nondimensional system of governing equations [48]:

$$\nabla \cdot \mathbf{u}^* = 0, \quad (11)$$

$$\begin{aligned} \frac{\partial \rho^* \mathbf{u}^*}{\partial t^*} + \nabla \cdot (\rho^* \mathbf{u}^* \mathbf{u}^*) \\ = \nabla \cdot \mu^* \nabla \mathbf{u}^* - \nabla p^* + U \mathbf{F}_e^* + \rho^* \mathbf{g}^* + \frac{\mathbf{g}^*}{\text{Bo}} (\nabla_s \cdot \mathbf{n}), \end{aligned} \quad (12)$$

$$\mathbf{E}^* = -\nabla \phi^*, \quad (13)$$

$$\nabla \cdot (\varepsilon^* \nabla \phi^*) = -\rho_e^*, \quad (14)$$

$$\frac{M}{U^{1/2}} \frac{\partial \rho_e^*}{\partial t^*} + \frac{M}{U^{1/2}} \nabla \cdot (\rho_e^* \mathbf{u}^*) + \nabla \cdot (\rho_e^* K^* \mathbf{E}^*) = 0. \quad (15)$$

The superscript “ $*$ ” represents the dimensionless values of the corresponding entities. Adopting the treatment in Ref. [48], the properties of liquid (ρ_l , μ_l , ε_l , K_l) are chosen as characteristic properties (ρ_c , μ_c , ε_c , K_c). For the convenience of expression, we define the dimensionless total charge transport velocity as $\mathbf{u}_t^* = \frac{M}{U^{1/2}} \mathbf{u}^* + K^* \mathbf{E}^*$. Other nondimensional parameters that are defined to facilitate the analysis are expressed as follows:

$$g^* = \frac{\rho_c^2 D^3}{\mu_c^2} g, \quad \text{Bo} = \frac{\rho_c g D^2}{\sigma}, \quad M = \frac{1}{K_c} \sqrt{\frac{\varepsilon_c}{\rho_c}}, \quad U = \frac{\varepsilon_c \rho_c V^2}{\mu_c^2}. \quad (16)$$

Here g^* can be treated as a nondimensional measure for the acceleration due to gravity. Bo is the Bond number, which represents the ratio of gravitational force to the surface tension force. M is the ratio of the so-named hydrodynamic mobility to ionic mobility. The parameter U represents the ratio of electric force to viscous force and it serves as the driving parameter for the present system. The corresponding nondimensional boundary conditions at electrodes are as follows:

$$\begin{aligned} \mathbf{u}^* = 0, \quad \phi^* = 1, \quad \rho_e^* = C \text{ at } y^* = 1 + L^*, \\ \mathbf{u}^* = 0, \quad \phi^* = 0 \text{ at } y^* = 0, \end{aligned} \quad (17)$$

where $C = \rho_{e0} D^2/\varepsilon_c V$ is a parameter that serves an indication for the injection strength and $L^* = L/D$ denotes the nondimensional thicknesses of the air layer. Meanwhile, in order to highlight the role of each dimensionless parameter at the interface, the dimensionless form of Eq. (10) is also given as:

$$[\mathbf{E}^*] \times \mathbf{n} = 0, \quad [\varepsilon^* \mathbf{E}^*] \cdot \mathbf{n} = 0, \quad [K^* \mathbf{E}^* \rho_e^*] \cdot \mathbf{n} = 0, \quad (18a)$$

$$\mathbf{t} \cdot (\nabla \mathbf{u}^* + \nabla \mathbf{u}^{*T}) \cdot \mathbf{n} = 0, \quad (18b)$$

$$\begin{aligned} - [p^*] + \mathbf{n} \cdot (\nabla \mathbf{u}^* + \nabla \mathbf{u}^{*T}) \cdot \mathbf{n} + U [\varepsilon^* (\mathbf{E}^* \cdot \mathbf{n})^2] \\ - U [\frac{1}{2} \varepsilon^* E^{*2}] - \frac{g^*}{\text{Bo}} (\nabla_s \cdot \mathbf{n}) = 0. \end{aligned} \quad (18c)$$

III. NUMERICAL METHODOLOGY

The numerical model for the two-phase EHD problem presented in this work is built on the VOF method-based finite-volume framework of OpenFOAM [49]. The governing equations for the electric potential, electric field, charge

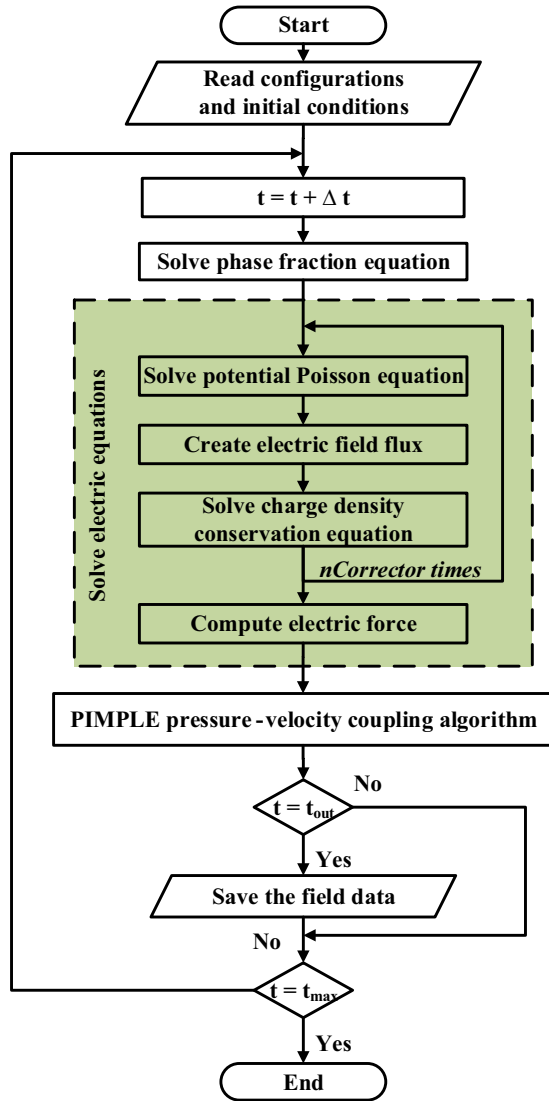


FIG. 2. Flow chart of the solution procedure. $nCorrectors$ times is the solving times of electric equations.

transport, and the expression for electric body force term are implemented into the framework. Meanwhile, since Eq. (10) is obtained by integrating the respective conservation equations across the interface, the conservative VOF method is able to ensure that the numerical solution satisfies Eq. (10) without explicit enforcement. A sequential, iterative solution procedure based on the PIMPLE algorithm [54] is employed to solve the discrete equations. Since the Poisson's equation and charge density conservation equation are coupled, an iterative subloop is designed to ensure full convergence and

enhance the solving stability. Figure 2 presents the overall solution procedure.

The governing equations are discretized using the standard finite-volume procedures available in OpenFOAM as described by Moukalled *et al.* [55]. The time derivatives are discretized using the Crank-Nicolson scheme with a weighting factor of 0.9. The Laplacian terms present in the governing equations are discretized using a second-order accurate central differencing scheme. A third-order cubic scheme is employed to discretize the gradient terms. The convective terms in the momentum and charge density conservation equations are discretized using the third-order QUICK scheme [56] while a second-order total variation diminishing (TVD) Van Leer scheme is employed [57] to discretize the convection term in the phase fraction equation. For the electromigration term, TVD Van Leer scheme is also used to get accurate charge density distribution near the electrode [58]. OpenFOAM also introduces an interface compression term in Eq. (7) to sharp the interface [59,60] and this term is discretized with central scheme.

IV. RESULTS AND DISCUSSION

This work primarily presents a numerical investigation of EHD stability of a dielectric liquid with horizontal liquid-air interface exposed to a vertical electric field. The process of charge transport under electrohydrostatic equilibrium state and the instability feature as well as the flow pattern are systematically studied.

A. Choice of parameters and stability analysis

The geometrical configuration, boundary conditions, and governing parameters used in this study are basically adopted from the linear stability of Chicón and Pérez [48]. However, few parameters are set different from Ref. [48] in order to reduce the computational expenses. The parameters used in this study are summarized in Table I.

The first modification is to increase the ratio of ion mobility between the liquid layer and the air layer from 5×10^{-6} used by Chicón and Pérez to 1×10^{-2} . The usage of very small ionic mobility ratio leads to a high electromigration flux \mathbf{KE} in the air layer and low flux in the liquid. Thus, a very small time step (around 10^{-4} dimensionless time) as well as a long simulation time (around 10^4 to 10^5 dimensionless time) are required to achieve a divergence free numerical solution. Therefore, a greater ionic mobility ratio is considered to reduce simulation consumption. For the same purpose, the air and liquid layers are set to be of the same thickness in this paper while Chicón and Pérez [48] used an air layer which is 11.5 times thicker than the liquid layer. The instability

TABLE I. The parameters used in the previous linear stability analysis and the present study.

	Thickness of liquid layer	K_l/K_a	ϵ_l/ϵ_a	ρ_l/ρ_a	ν_l^a	C	Bo	g^*	M	L^*
Linear stability analysis [48]	1.2 mm	5×10^{-6}	2.73	800	5×10^{-5} m ² /s	10	0.678	6.78	317.36	11.5
Present study		1×10^{-2}								1.0

^aThe viscosity in the air layer is not required in the linear stability analysis since it ignores the flow in air. In our simulation, the viscosity of the air is set to be 1.57×10^{-5} m²/s.

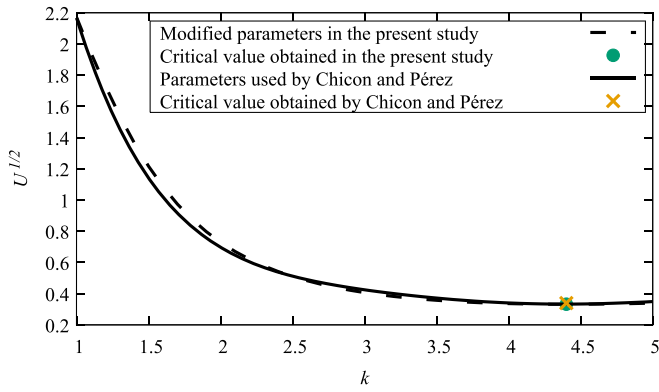


FIG. 3. The instability diagrams with the original and changed parameters.

diagram plotted using the parameters used in Ref. [48] shows a good agreement with the instability diagram obtained using the modified parameters in this study (Fig. 3). For details of the stability analysis process, please refer to Ref. [48]. The critical values obtained using the modified parameters are $U_c = 0.1106$ and $k_c = 4.4$ which are close to the critical values $U_c = 0.1155$ and $k_c = 4.4$ obtained by using the parameters considered by Ref. [48]. Thus, it is confirmed that the modified parameters used in this study do not alter the key stability characteristics of the liquid layer.

To understand why the adjustment of air layer parameters has no significant effect on the stability of the system, the role of air-liquid interface in this problem needs to be discussed. In the stability analysis, the air layer is considered to be in electrohydrodynamic equilibrium because of the large ion mobility in the air layer [48]. Therefore, the instability of the system is dominated by the liquid layer and the interface acts as a flexible electrode plate boundary for the liquid layer. In the mechanics part, the relations at interface have not changed since the velocity in the air layer is assumed to be zero in the stability analysis. In the electrical part, the change of ion mobility in the air layer will affect the charge accumulation at the interface. However, the charge density in the liquid layer has already become saturated due to the high charge injection intensity. Thus, the limited change of charge accumulation at interface has negligible effect on the electric field characteristics in the liquid layer. As a result, the stability feature shown in Fig. 3 has not changed.

B. Electrohydrostatic equilibrium regime

The present flow problem exhibits an electrohydrostatic regime when the driving parameter U is kept smaller than the critical value. In this regime, the electric body force is weak and cannot induce any motion in the liquid region and thus the system remains in a rest state. An analytical solution for the charge density, electric field distribution, and pressure in

TABLE II. The constants in the equations of static solution.

a	b	c	d
0.211738	$1 + 1.5038701 \times 10^{-5}$	1.281494	0.003663

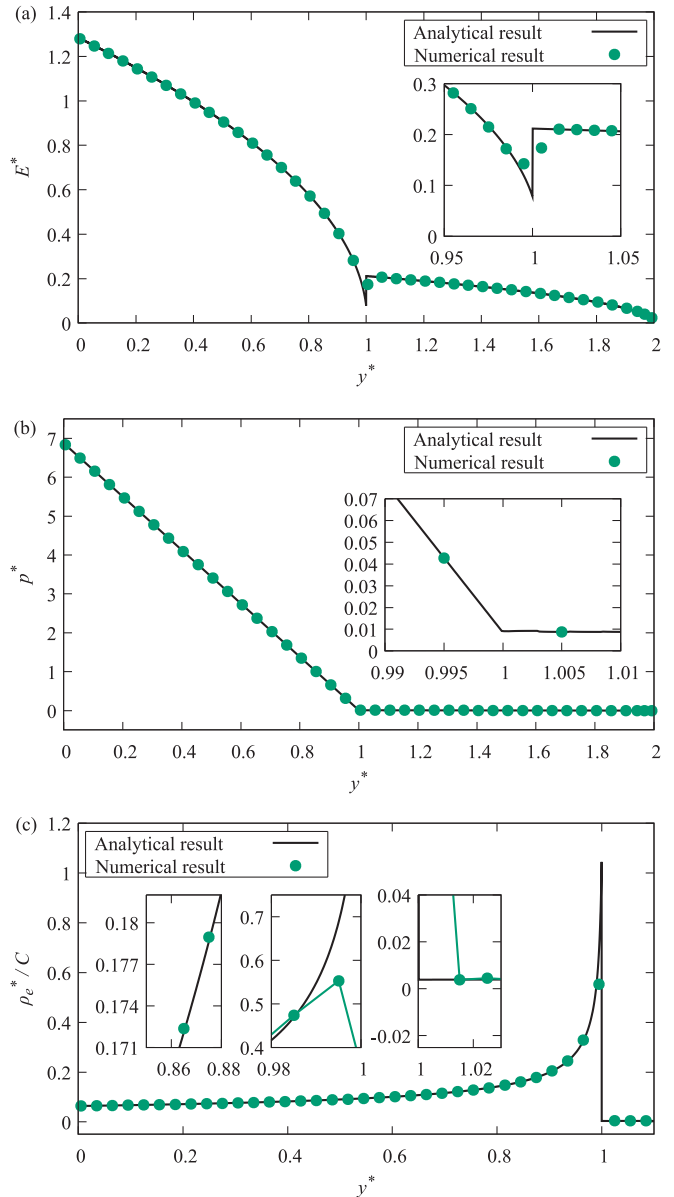


FIG. 4. Comparison of numerical results from present work with analytical solutions in electrohydrodynamic equilibrium condition along the y direction. (a) Electric field strength. (b) Pressure. (c) Charge density.

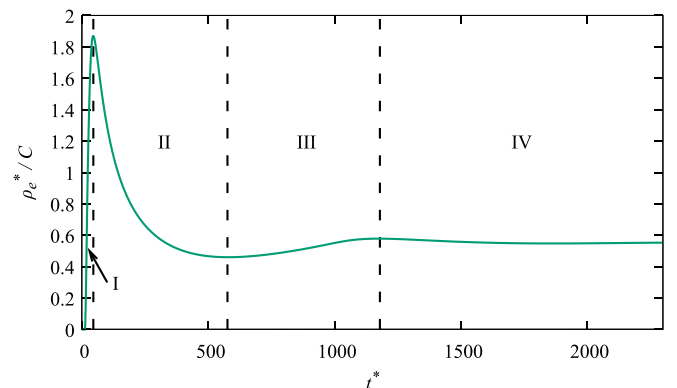


FIG. 5. Time evolution of charge density in the mesh cell closest to the interface in the liquid layer.

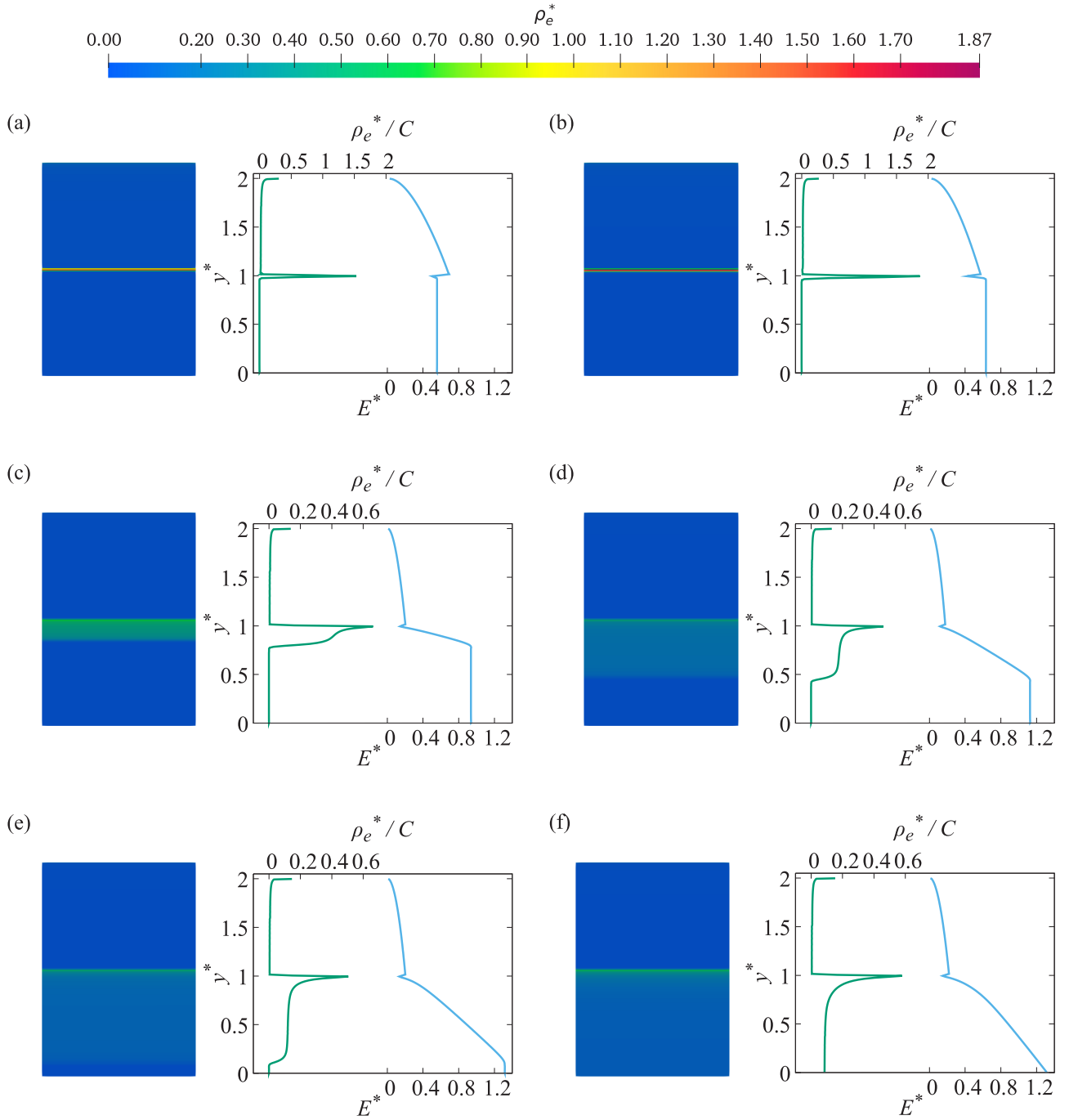


FIG. 6. The charge density (green line) and electric field strength (blue line) distributions during the injection process with $U = 0.10$. When $t^* = 44.4$, the charge density near the interface reaches its peak value, while it reaches its bottom value at $t^* = 576$. (a) $t^* = 30$, in stage I. (b) $t^* = 44.4$, at the boundary between stages I and II. (c) $t^* = 250$, in stage II. (d) $t^* = 576$, at the boundary between stages II and III. (e) $t^* = 850$, in stage III. (f) $t^* = 1180$, at the boundary between stages III and IV.

the electrohydrostatic regime is given below [48]:

$$E_l^* = c\sqrt{(1-y^*+d)}, \quad E_a^* = a\sqrt{(1-y^*+b)}, \quad (19a)$$

$$\rho_{el}^* = \frac{c}{2\sqrt{(1-y^*+d)}}, \quad \rho_{ea}^* = \frac{a\varepsilon_a}{2\varepsilon_l\sqrt{(1-y^*+b)}}, \quad (19b)$$

$$p_l^* = P_{0l}^* + (g^* + UJ_0)(1-y^*),$$

$$p_a^* = P_{0a}^* + \left(\rho^*g^* + UJ_0\frac{1}{K^*}\right)(1-y^*+L). \quad (19c)$$

In Eq. (19c), P_{0l}^* and P_{0a}^* are the initial parameters determined by the pressure near one of the electrodes and the pressure jump at the interface. J_0 is the nondimensional current density defined as $J_0 = K^*E^*\rho_e^*$. The coefficients a , b , c , d presented in Table II are constants determined with the parameters listed in Table I. The values of a , c , and d are related to (1-b), and thus b needs to have high accuracy. Figure 4 presents a comparison of our numerical solution with the analytical solution in the electrohydrostatic regime. A nonuni-

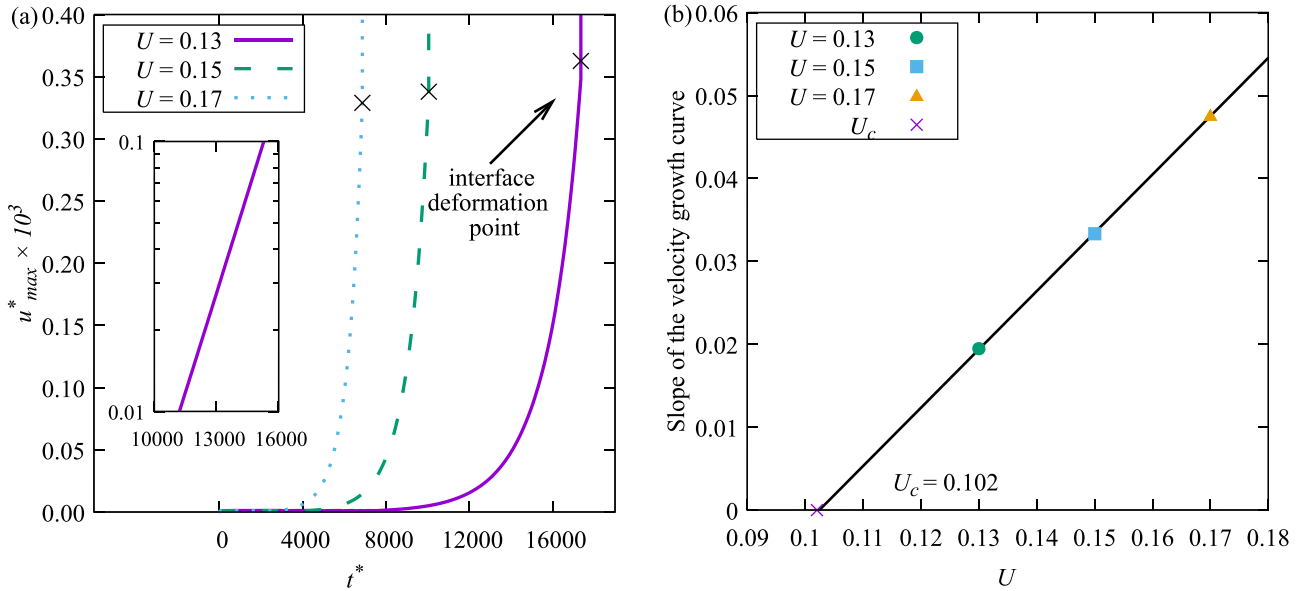


FIG. 7. Variation of the maximal velocity U_{max} with different driving parameters U . (a) The maximum velocity in the liquid layer. Logarithmic coordinates are used to show the exponential growth rate of the velocity in the insert diagram. (b) The linear relationship between the exponential growth rate and driving parameter when U is close to U_c .

form grid that has been refined near the injection electrode is used in our numerical procedure. There are 200 cells in the vertical direction before refinement which is proved to be mesh independent(see Appendix). The numerical results for the distributions of electric field, pressure, and charge density exhibit a good agreement with the analytical solution.

Figure 5 presents the charge density evolution with time near the interface, starting with all zero fields in the bulk. Accordingly, the profiles of E^* and ρ_e^* across the interface at some selected moments are presented in Fig. 6. In stage I where $t^* < 44.4$, the charge accumulates near the interface and it is observed that the charge does not penetrate much deeper into the liquid layer. Then in stage II where $44.4 \leq t^* \leq 576.0$, the charge accumulation near the interface reaches a very high value and the charge distribution begins to seep into the liquid region. The charge density near the interface depends on the balance between the electromigration velocity in the liquid and air layer. From Eq. (4) and Eq. (5) we can obtain that once the charge is injected into liquid, the corresponding electric field strength E_l will increase and finally cause the growth of the migration velocity $K_l E_l$ in the liquid layer. This increase breaks up the original balance of migration velocities on both sides of the interface and results in the rapid drop of the interface charge density. However, with the further charge transport to the liquid layer, the electric field strength on the liquid side of the interface decreases gradually [as shown in Fig. 6(c) and Fig. 6(d)]. Due to the decreased migration velocity caused by the fall in electric field strength in liquid region, the charge transport velocity in the air layer dominates again. Then, the charge density near the interface again begins to shoot up and this stage is marked as stage III [$576 \leq t^* \leq 1180$, from Fig. 6(e) to Fig. 6(f)]. When the charge reaches the collector electrode, the last stage ($1180 < t^*$, stage IV in Fig. 5) begins. Electric

field and charge distribution in the liquid layer will undergo an adjustment process to achieve the final state.

C. Stability threshold and flow pattern

The fluid motion will occur if the driving parameter U is greater than the critical value. To study the flow pattern near the stability criterion, the width of the flow domain near the stability criterion, the width of the flow domain in our simulation is considered to be 1.43 times the thickness of the liquid layer, corresponding to the critical wavelength. The variation of the maximum velocity within the liquid layer with respect to the driving parameter U is presented in Fig. 7(a). The liquid layer, which is at an equilibrium state, gradually evolves into a dynamic state. It is observed that the time evolution curve of the maximum velocity undergoes an exponential growth after an initial period of latency. The corresponding linear stability criterion can be estimated using the growth rate of the curve as presented in Refs. [61–63]. Following this approach, the velocity growth curve with respect to the parameter U is plotted in Fig. 7(b). The critical value of U is calculated as 0.102, which matches well with the analytical result. The flow pattern and its formation mechanism are presented in Fig. 8 and Fig. 9, respectively. First, as shown in Fig. 8(a) and Fig. 9(a), the velocity owns an upward component between two vortices. This direction is opposite to the local electric field, and thus the total transport velocity of charge $K\mathbf{E} + \mathbf{u}$ is weaker there [Fig. 8(b)]. Meanwhile, since the charge flux injected from the interface remains unchanged, the weakened transport velocity in the bulk finally results in a charge accumulation area near the interface and a thin charge region between vortices [Fig. 8(c) and Fig. 9(b)]. The thinner charge in turn reduces the local electric strength \mathbf{E} according to $\nabla \cdot \epsilon \mathbf{E} = \rho_e$ derived from Eq. (4) and Eq. (5), which decreases the total transport velocity of charge $K\mathbf{E} + \mathbf{u}$ on the

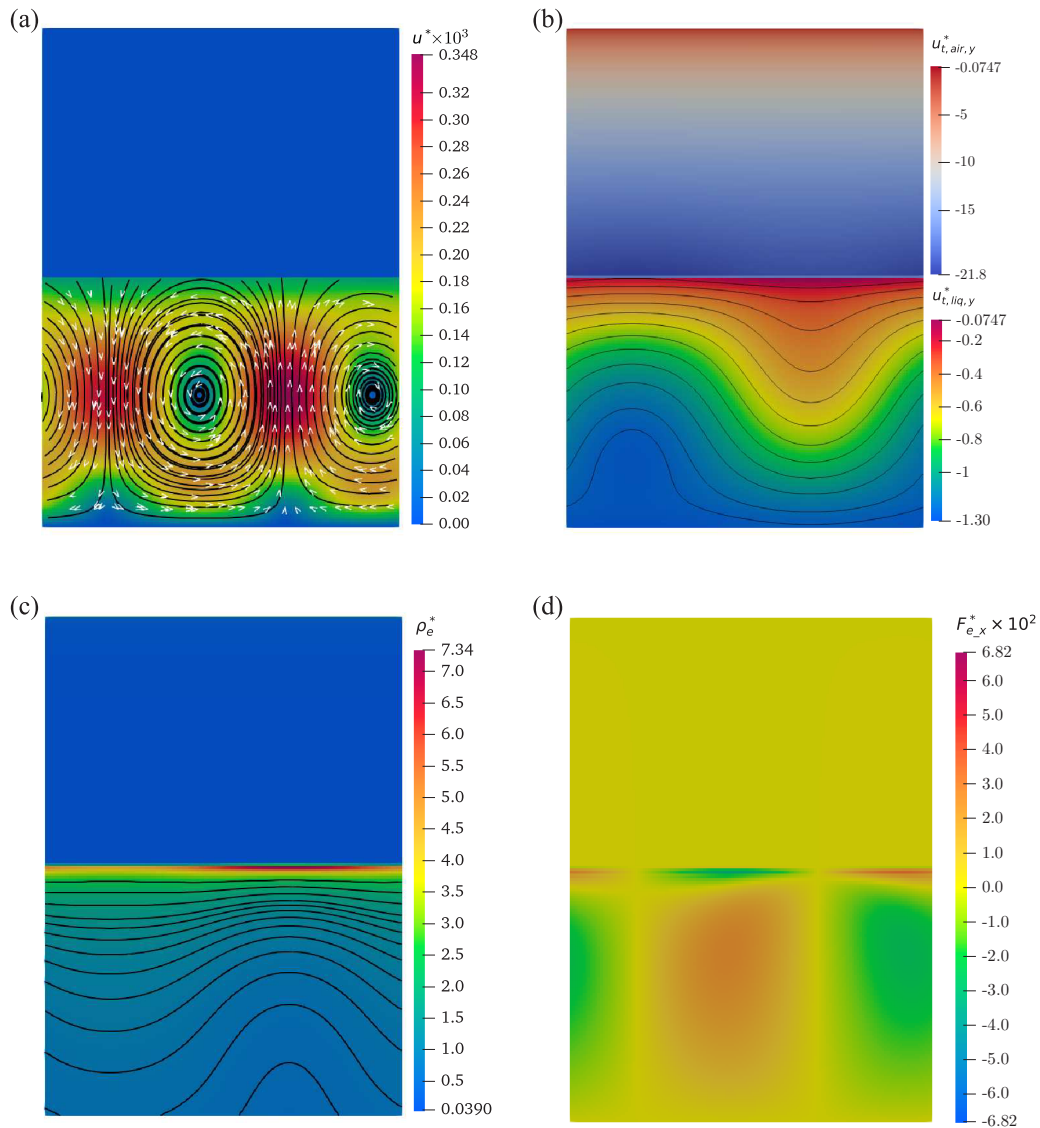


FIG. 8. The cloud chart of each dimensionless physical quantity at the moment just before the interface deformation with $U = 0.13$. (a) The distribution of velocity with corresponding streamline. (b) The distribution of total transport velocity with corresponding isoline. Since the total transport velocity in the air layer is much larger than the value in the liquid layer, another color scale is used in the air layer. (c) The distribution of charge density with corresponding isoline. (d) The distribution of tangential electric force.

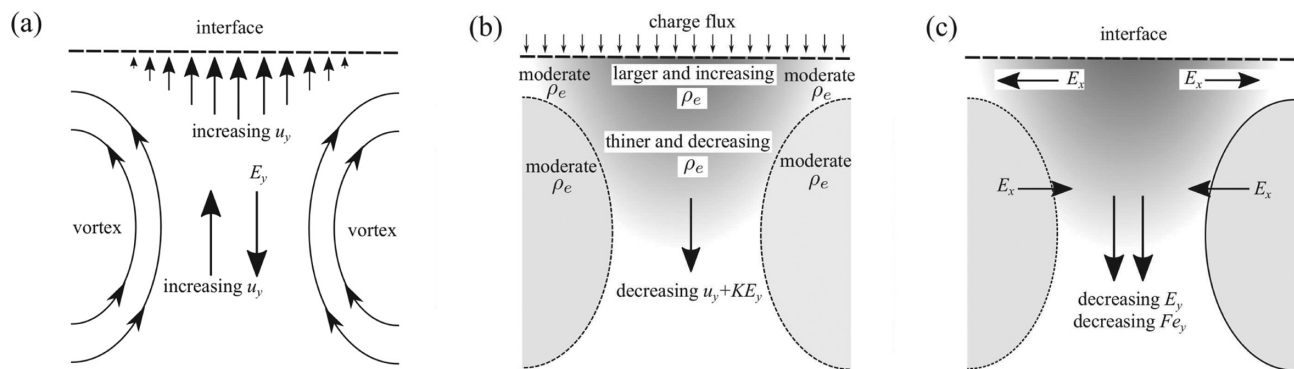


FIG. 9. The sketch of the flow pattern development process. (a) The velocity distribution induced by the vortex flow. (b) The ununiform charge density distribution caused by the ununiform charge transportation. (c) The shear distribution of electric field due to the uneven charge density.

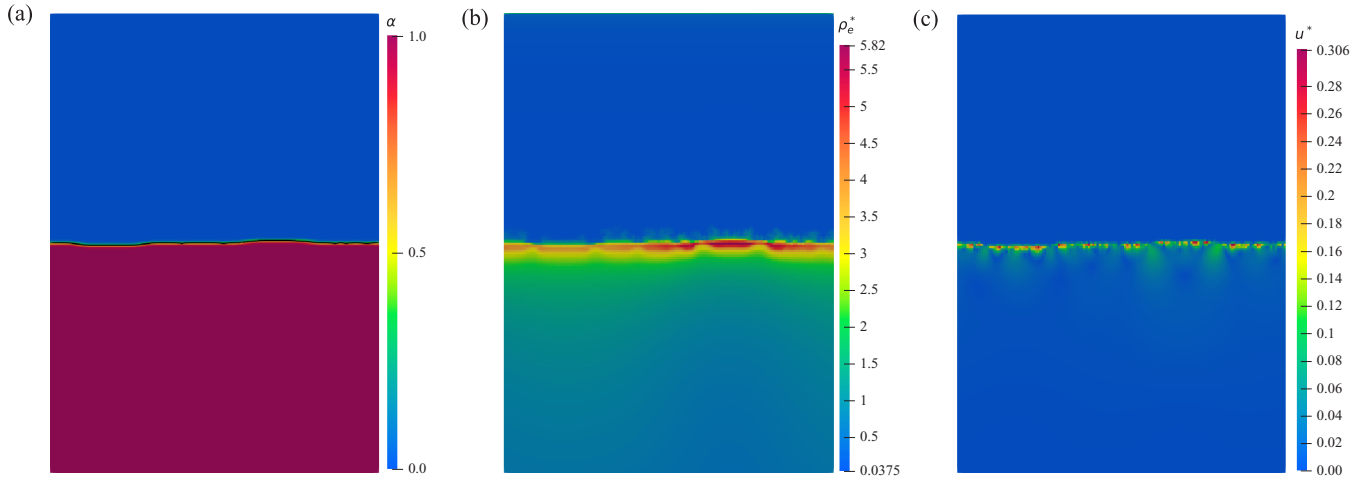


FIG. 10. The interface deformation and corresponding charge distribution with $U = 0.13$. (a) The irregular interface deformation. A solid black line is used to distinguish the interface. (b) The distribution of irregular charge. (c) The distribution of velocity.

one hand and decline of the Coulomb force $\rho_e \mathbf{E}$ on the other hand [Fig. 9(c)]. The reduced Coulomb force between vortices increases the local velocity correspondingly since the opposite direction they owned [Fig. 9(a)], and the above process will be staged again, establishing an unstable positive cycle.

Besides, the charge between the vortex is weakened and the charge near the interface is enhanced, while the charge density in the center of the vortex is basically unaffected [Fig. 9(b)]. This kind of charge density distribution results in the opposite direction of horizontal electric field in the corresponding region [Fig. 9(c)], which eventually leads to the shear distribution of tangential electric force near the interface [Fig. 8(d)]. In Sec. IV D, we will show that this shear distribution exists only in a two-phase system. Since the surface tension is always perpendicular to the interface, the tangential electric force getting larger with the growth of the vortex strength can only be balanced by finite viscous stress, which is a possible mechanism behind interface instability. However,

before this mechanism works, the up-flow component in the vortex will deform the interface first. It makes the interface where the highest charge density is seen to protrude upward (see Fig. 8). The deformation time is marked in the velocity curve in Fig. 7(a) and the charge at interface will no longer be stable after the interface's deformation. The unstable charge density leads to more irregular deformation of the interface, as seen in Fig. 10. After the appearance of the surface deformation, the liquid velocity will jump by several orders, as seen in Fig. 10(c), and the system will become more and more chaotic as time increases.

D. The charge void region and the effect of the slip boundary at interface

It is worthwhile to first emphasize that the slip boundary condition mentioned here refers to the role of the interface for the liquid layer rather than the boundary conditions required

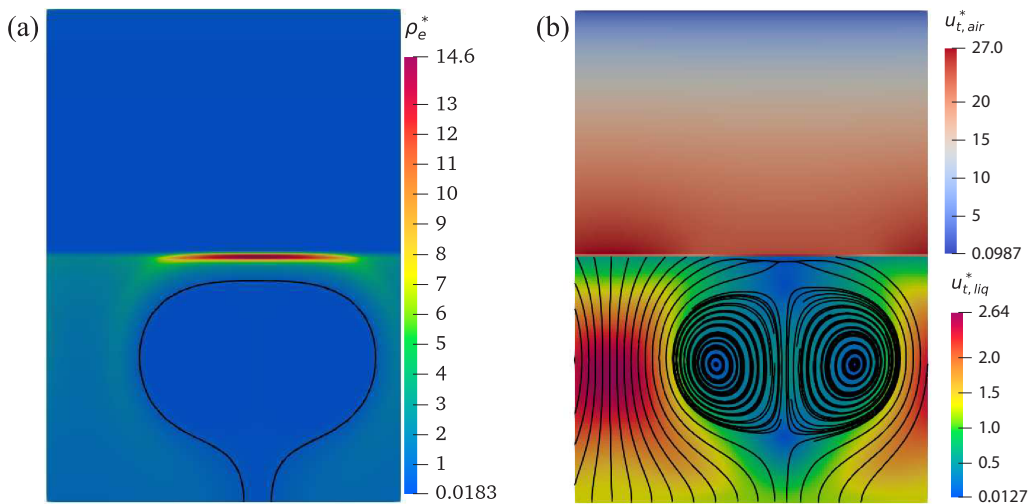


FIG. 11. The charge and total transport velocity distribution in the domain when $U = 0.12$. (a) The charge void region with the black line as the isoline of $\rho^* = 0.5$. (b) The total transport velocity distribution with corresponding streamline. Since the total transport velocity in the air layer is much larger than the value in the liquid layer, another color scale is used in the air layer.

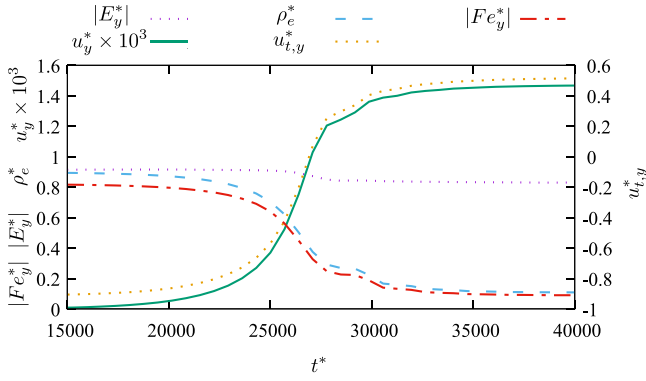


FIG. 12. Time evolution of dimensionless electric field, charge density, electric force, velocity, and total transport velocity of charge with the ordinate of $y^* = 0.5$ at junction of two vortices when $U = 0.12$.

by the numerical solution of the governing equations. The interface is completely located in the computational domain in our numerical procedure, and we have mentioned in Sec. III that the relationship between physical quantities at the interface can be guaranteed by the VOF method. The existence of the interface brings two new factors, deformability and the slip boundary condition, to the system. In order to study the effect of slip boundary conditions at the interface separately, the phase fraction equation Eq. (7) is blocked in this section. This does not change the boundary conditions at the interface while keeping the interface undeformed. The so-called charge void region shown in Fig. 11(a) then can be captured without the phase update code. The occurrence of this structure is the result of a positive cycle illustrated in Fig. 9 before, which is interrupted by interface deformation in early cases as described in previous section. To further illustrate this positive cycle, Fig. 12 shows the time evolution of the related variables at the region near the interface with $U = 0.12$. As shown in this figure, the growth of the velocity is accompanied by the decrease of total charge transport velocity $|u_{t,y}^*|$, limiting the amount of charge

injected into the liquid layer. Meanwhile, thinner charge in turn reduces the local electric field value. This not only causes the further reduction of the magnitude of $|u_{t,y}^*|$ but also reduces the local electric force, which further increases the local velocity again. Finally, the total charge transport velocity $u_{t,y}^*$ turns its direction and the charge can no longer be injected into the deeper liquid; the system reaches a steady state. The final distribution of the whole dimensionless charge transport velocity is given in Fig. 11(b) and the self closed streamline of total velocity in the figure shows that no free charge can be injected into or escape from the charge void region.

The key characteristic of EHD-related convection, the subcritical bifurcation, is also observed in this study. As shown in Fig. 13(a), the system will remain at rest when the simulation is started with a small driving parameter U . With the increase of U , the stable convection cell as well as the charge void region will occur when $U > U_c$. This critical value corresponds to the linear stability criterion. The strength of the flow will gradually weaken when U is decreased from a steady convection until it meets another critical value, where the motion suddenly stops. This criterion is marked as U_f as it is related to finite-amplitude instability. We numerically found $U_f = 0.059$. Since U_f is smaller than U_c , a hysteresis curve is established as presented in Fig. 13(a). The hysteresis of the single-phase case is also plotted in Fig. 13(b) for comparison. The shape of the charge void region with driving parameters both greater and less than U_c is shown in Fig. 14. Since the electric torque which drives the flow is proportional to the size of the void region [35], the void region area owns a nonzero value when $U = 0.06$ which is close U_f . The width and height of the charge void region become smaller with the decrease of driving parameters while the neck of the region becomes larger. When U lies between the two critical values, the profile changes more sharply than when the driving parameter is less than the U_c . This variation is consistent with the results of a single-phase EHD convection [64].

The charge void region in two-phase system exhibits some key differences from a single-phase EHD problem. To illustrate this point, we show the charge void regions both formed

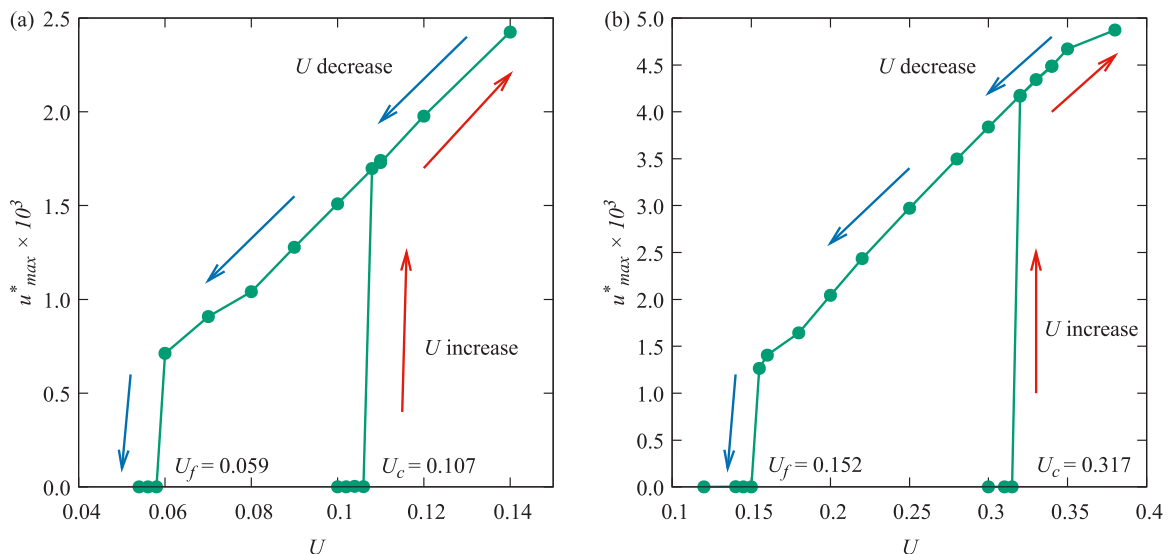


FIG. 13. Comparison of hysteresis loop in two-phase and single-phase system. (a) Two-phase system. (b) Single-phase system.

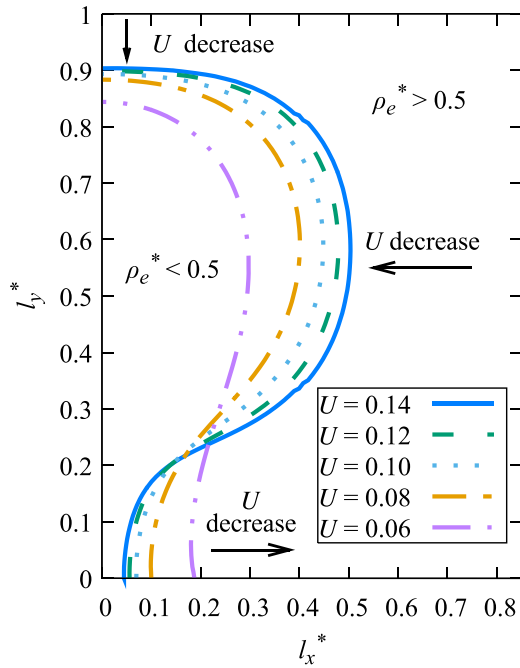


FIG. 14. The isoline of $\rho_e^* = 0.5$ with different drive parameters.

by the single-phase electroconvection and the two-phase flow in Fig. 15. The two charge void regions are simulated with the same driving parameters. Key differences between two charge void regions can be summarized as follows. First, the void region in the two-phase system has a larger size, which means the convection strength is greater. This can also be related to Fig. 13 where the single-phase case shows a much higher linear and nonlinear critical values. Second, the upper edge of the charge void region coincides with the interface in the two-phase system while there exists a notable gap between the void region and the interface (electrode) in a single-phase case. This can be explained by the velocity boundary conditions

at interface and rigid electrode. The interface acts as a slip boundary condition since the velocity is continuous between the movable air and liquid, which allows vortex structure in the liquid layer extend to the interface. While the viscous effect near the no-slip electrode forces the vortex to stay away from the injection electrode for a single-phase problem. This viscous effect is also the main reason for the smaller charge void region in single-phase flow. Third, the charge density at the interface exhibits a much higher peak value and horizontal gradient in air-liquid system. This phenomenon can be understood from two aspects. On the one hand, the convection strength is much larger in the presence of an interface, which makes the flow have a stronger influence on charge distribution. On the other hand, since the charge cannot be transported into charge void region due to the self-closed total migration velocity [Fig. 11(b)], the interface closely connected with the void region in air-liquid system cannot inject enough charge to the liquid layer, which makes it easier for that part of interface to accumulate more charge from the upper layer. Moreover, just as in the discussion in Sec. IV C and Fig. 9, the higher peak value and horizontal gradient in the air-liquid system causes the horizontal component of the electric force to change the direction near the interface, forming a shear electric field force distribution. However, as shown in Fig. 16, the shear electric force is absent in the single-phase system since no notable transverse gradient of charge distribution exists near the interface, which shows that the slip interface is a necessary condition for the formation of shear electric force.

Overall, it can be inferred that the absence of viscous effect at interface allows for a finite velocity there, which makes it easier for the flow to develop and generate a larger flow intensity, resulting in a smaller critical value than single-phase system. The structure of the charge void region is also effected by the stronger flow and the velocity at interface. The velocity slip boundary condition at the interface is the reason for the formation of shear electric field force near the interface, which makes the interface prone to deformation.

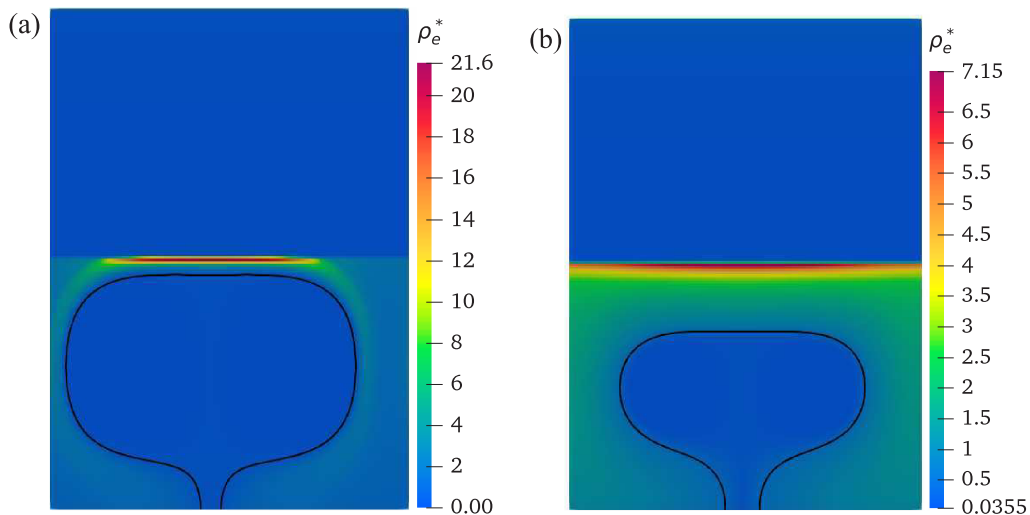


FIG. 15. Comparison of charge void region in two-phase and single-phase system with $U = 0.35$. (a) Two-phase system. (b) Single-phase system.

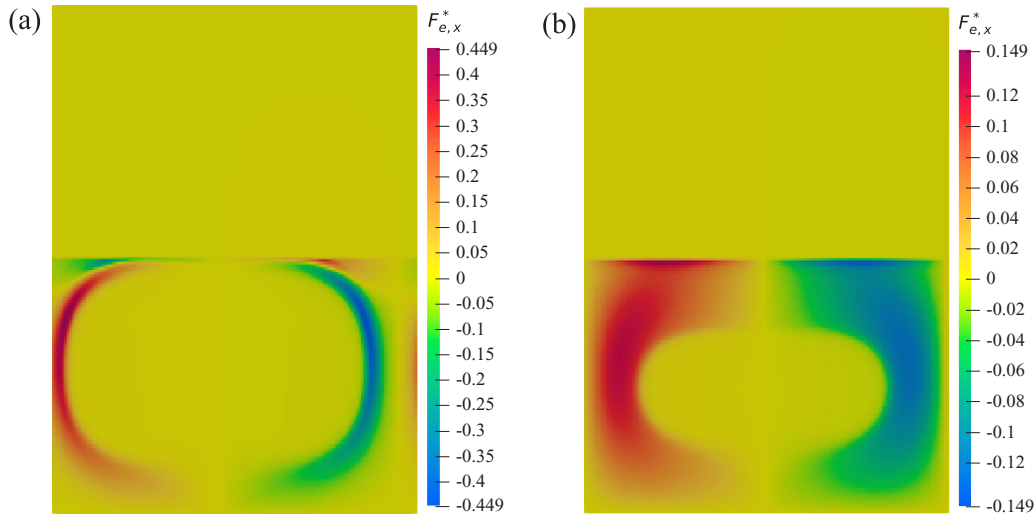


FIG. 16. Comparison of tangential electric force in two-phase and single-phase system with $U = 0.35$. (a) Two-phase system. (b) Single-phase system.

V. CONCLUDING REMARKS

In this paper, two-dimensional numerical simulation was performed to study the EHD instability with a planar layer of air-dielectric liquid subjected to unipolar injection. This fundamental two-phase EHD problem has been investigated with the linear stability tool, and this study presents direct numerical results for the first time. A finite volume solver with the electrostatic equations implemented in the open-source platform OpenFOAM was developed, and the VOF model was used to deal with the liquid-air interface. The solver was first validated by the electrohydrostatic equilibrium solution. Then numerical results with the onset of flow motion and flow structure were presented. The numerically obtained critical value for the linear stability matches well with the theoretical values. Once the flow develops, the interface deformation becomes irregular, and the resulting flow structure and charge void region is chaotic.

One of the most important contributions of this study is to give the differences between single-phase system and two-phase system caused by the slip interface. On the one hand, the lack of viscous effect at the free interface accounts for the smaller instability threshold in two-phase system compared with the single-phase case. The linear criterion is $U_c = 0.107$, which agrees well with the analytical solution. Meanwhile, the finite-amplitude criterion with the blocked deformation and slip interface, corresponding to the stop of flow motion, was obtained as $U_f = 0.059$. This discovery provides a possibility to improve the flow intensity in some industrial applications. For example, in electric field-enhanced heat transfer, using a two-phase film instead of a single-phase liquid can reduce the voltage threshold of flow, obtain higher flow intensity at the same voltage, and thus obtain higher heat transfer efficiency. On the other hand, the presence of interface also changes the flow pattern. The slip interface enlarges the size of charge void region and shifts its position closer to the interface. The distribution of tangential electric force near the interface and its formation mechanism are described. It is considered that this distribution will only occur with a slip boundary. This finding

can help us get a better understanding on some EHD flows in presence of a free surface like Rose window instability where the electric stress might have a vital role forming a beautiful interface deformation pattern.

Though the present study and also previous stability analysis [48] are inspired by the Rose window instability, the experimental condition of needle-plate electrode configuration and much higher values of driving parameter bring some inherent differences and challenges. The 3D simulation of Rose window instability phenomenon can be a future work.

ACKNOWLEDGMENTS

J.W. acknowledges financial support by the National Natural Science Foundation of China via Grants No. 11802079 and No. 12172110. A.T.P. acknowledges financial support by the Spanish Ministerio de Ciencia, Innovación y Universidades under Research Project No. PGC2018-099217-B-I00, by the Ministerio de Economía y Competitividad under Research Project No. CTQ2017-83602-C2-2-R, and Junta de Andalucía under Research Project No. 2019/FQM-253.

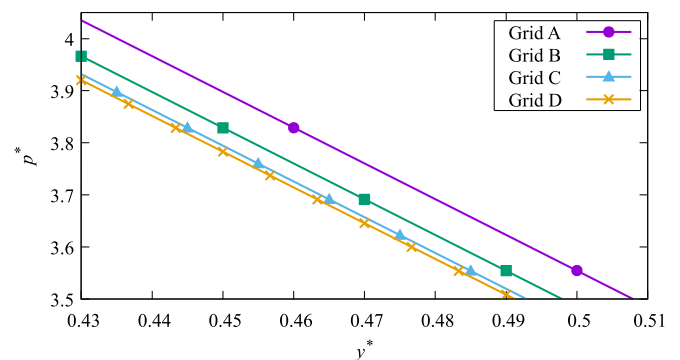


FIG. 17. The pressure distribution in liquid layer with different grids.

TABLE III. The numerical result with different grids^a.

	Grid A	Grid B	Grid C	Grid D
J^*	0.81696	0.81918	0.82017	0.82039
Relative error of J^*	–	0.27%	0.12%	0.03%
Relative error of p^*	–	1.96%	1.01%	0.32%
$u_{\max}^* \times 10^3$	3.08748	5.48995	6.77753	6.62854
Relative error of u_{\max}^*	–	77.81%	23.45%	2.20%

^aThe relative error is defined as $[(J^*, p^*, \int_{\text{liquid}} p^* dy^*)_c - (J^*, p^*, \int_{\text{liquid}} p^* dy^*)_r] / (J^*, p^*, \int_{\text{liquid}} p^* dy^*)_r$ where the subscript “c” is the value of the current grid and “r” is the value of the rougher grid.

APPENDIX: GRID INDEPENDENT STUDY

Four different orthogonal grids named (1) grid A (36 × 50), (2) grid B (72 × 100), (3) grid C (144 × 200), and (4) grid D (216 × 300) with mesh refinement at $L/15$ away from the injection electrode are used to perform the simulations. Dimensionless current density $J^* = K^* E^* \rho_e^*$, dimensionless pressure distribution under static solution with the drive parameter $U = 0.10$, as well as the maximum velocity in liquid

layer with $U = 0.35$ (the case of Fig. 15) are used as electric-ity and mechanics evaluation indexes. The results are shown in Fig. 17 and Table III.

With the increase of grid density, the current density and pressure show few changes while the maximum velocity improves a lot. When the grid is encrypted from grid C to grid D, the result improvement is very limited. Considering both the accuracy and the consumption of simulation resources, grid C is chosen as the final grid for simulations.

[1] J. R. Melcher and G. I. Taylor, Electrohydrodynamics: A review of the role of interfacial shear stresses, *Annu. Rev. Fluid Mech.* **1**, 111 (1969).

[2] O. Schnitzer and E. Yariv, The Taylor-Melcher leaky dielectric model as a macroscale electrokinetic description, *J. Fluid Mech.* **773**, 1 (2015).

[3] P. M. Vlahovska, Electrohydrodynamics of drops and vesicles, *Annu. Rev. Fluid Mech.* **51**, 305 (2019).

[4] D. T. Papageorgiou, Film flows in the presence of electric fields, *Annu. Rev. Fluid Mech.* **51**, 155 (2019).

[5] B. Dinesh and R. Narayanan, Nature of branching in electrohydrodynamic instability, *Phys. Rev. Fluids* **6**, 054001 (2021).

[6] H. T. Yudistira, V. D. Nguyen, P. Dutta, and D. Byun, Flight behavior of charged droplets in electrohydrodynamic inkjet printing, *Appl. Phys. Lett.* **96**, 023503 (2010).

[7] G. J. McGranaghan and A. J. Robinson, The mechanisms of heat transfer during convective boiling under the influence of AC electric fields, *Int. J. Heat Mass Transf.* **73**, 376 (2014).

[8] A. M. Gañán-Calvo, J. M. López-Herrera, M. A. Herrada, A. Ramos, and J. M. Montanero, Review on the physics of electro-spray: From electrokinetics to the operating conditions of single and coaxial Taylor cone-jets, and AC electro-spray, *J. Aerosol Sci.* **125**, 32 (2018).

[9] P. A. Vázquez, M. Talmor, J. Seyed-Yagoobi, P. Traoré, and M. Yazdani, In-depth description of electrohydrodynamic conduction pumping of dielectric liquids: Physical model and regime analysis, *Phys. Fluids* **31**, 113601 (2019).

[10] W. Grassi and D. Testi, A new hydrodynamic approach for jet impingement boiling CHF, *Int. Commun. Heat Mass Transfer* **104**, 83 (2019).

[11] A. Ould El Moctar, N. Aubry, and J. Batton, Electrohydrodynamic micro-fluidic mixer, *Lab Chip* **3**, 273 (2003).

[12] B. Khorshidi, M. Jalaal, and E. Esmaeilzadeh, Electrohydrodynamic instability at the interface between two leaky dielectric fluid layers, *Colloids Surf., A* **380**, 207 (2011).

[13] R. Heidari, A. R. Khosroshahi, B. Sadri, and E. Esmaeilzadeh, The Electrohydrodynamic mixer for producing homogenous emulsion of dielectric liquids, *Colloids Surfaces A* **578**, 123592 (2019).

[14] G. I. Taylor and A. D. Mcewan, The stability of a horizontal fluid interface in a vertical electric field, *J. Fluid Mech.* **22**, 1 (1965).

[15] E. Schaffer, T. Thurn-Albrecht, T. P. Russell, and U. Steiner, Electrically induced structure formation and pattern transfer, *Nature (Lond.)* **403**, 874 (2000).

[16] K. Mondal and D. Bandyopadhyay, Electro-capillary instabilities of thin leaky elastic-viscous bilayers, *Phys. Fluids* **26**, 122006 (2014).

[17] K. Mondal, A. Ghosh, J. Chaudhuri, and D. Bandyopadhyay, Electric-field-mediated instability modes and Freedericksz transition of thin nematic films, *J. Fluid Mech.* **834**, 464 (2018).

[18] R. Cimpeanu, D. T. Papageorgiou, and P. G. Petropoulos, On the control and suppression of the Rayleigh-Taylor instability using electric fields, *Phys. Fluids* **26**, 022105 (2014).

[19] Q. Yang, B. Q. Li, Z. Zhao, J. Shao, and F. Xu, Numerical analysis of the Rayleigh-Taylor instability in an electric field, *J. Fluid Mech.* **792**, 397 (2016).

[20] Q. Yang, B. Q. Li, and F. Xu, Electrohydrodynamic Rayleigh-Taylor instability in leaky dielectric fluids, *Int. J. Heat Mass Transf.* **109**, 690 (2017).

[21] O. Ozen, N. Aubry, D. T. Papageorgiou, and P. G. Petropoulos, Monodisperse Drop Formation in Square Microchannels, *Phys. Rev. Lett.* **96**, 144501 (2006).

[22] S. Mählmann and D. T. Papageorgiou, Interfacial instability in electrified plane Couette flow, *J. Fluid Mech.* **666**, 155 (2011).

- [23] E. Dubrovina, R. V. Craster, and D. T. Papageorgiou, Two-layer electrified pressure-driven flow in topographically structured channels, *J. Fluid Mech.* **814**, 222 (2017).
- [24] R. Tomlin, R. Cimpanu, and D. Papageorgiou, Instability and dripping of electrified liquid films flowing down inverted substrates, *Phys. Rev. Fluids* **5**, 013703 (2020).
- [25] D. Tseluiko, M. G. Blyth, D. T. Papageorgiou, and J. M. Vanden-Broeck, Electrified viscous thin film flow over topography, *J. Fluid Mech.* **597**, 449 (2008).
- [26] D. Tseluiko, M. G. Blyth, D. T. Papageorgiou, and J. M. Vanden-Broeck, Electrified film flow over step topography at zero Reynolds number: an analytical and computational study, *J. Eng. Math.* **69**, 169 (2011).
- [27] A. W. Wray, D. T. Papageorgiou, and O. K. Matar, Electrified coating flows on vertical fibres: Enhancement or suppression of interfacial dynamics, *J. Fluid Mech.* **735**, 427 (2013).
- [28] P. Gambhire and R. M. Thakkar, Role of conductivity in the electrohydrodynamic patterning of air-liquid interfaces, *Phys. Rev. E* **86**, 036301 (2012).
- [29] L. Espin, A. Corbett, and S. Kumar, Electrohydrodynamic instabilities in thin viscoelastic films - AC and DC fields, *J. Non-Newtonian Fluid Mech.* **196**, 102 (2013).
- [30] A. Bandopadhyay and S. Hardt, Stability of horizontal viscous fluid layers in a vertical arbitrary time periodic electric field, *Phys. Fluids* **29**, 124101 (2017).
- [31] A. T. Pérez, Electrohydrodynamic instabilities in dielectric liquids induced by corona discharge, in *Proceedings of the 12th International Conference on Conduction and Breakdown in Dielectric Liquids (ICDL'96)* (IEEE, Los Alamitos, CA, 1996), pp. 126–129.
- [32] A. T. Pérez, Rose-window instability in low conducting liquids, *J. Electrostat.* **40**, 141 (1997).
- [33] P. Atten and D. Koulova-Nenova, EHD instability of insulating liquids due to charge injection from the free surface, in *Proceedings of the 12th International Conference on Conduction and Breakdown in Dielectric Liquids (ICDL'96)* (IEEE, Los Alamitos, CA, 1996), pp. 476–479.
- [34] D. Koulova-Nenova and P. Atten, EHD instability of air/liquid two layer system under unipolar charge injection, *J. Electrostat.* **40**, 179 (1997).
- [35] A. Castellanos, Coulomb-driven convection in electrohydrodynamics, *IEEE Trans. Electr. Insul.* **26**, 1201 (1991).
- [36] P. Atten, Electrohydrodynamic instability and motion induced by injected space charge in insulating liquids, *IEEE Trans. Dielectr. Electr. Insul.* **3**, 1 (2002).
- [37] P. Atten and R. Moreau, Stabilité électrohydrodynamique des liquides isolants soumis à une injection unipolaire, *J. de Méc.* **11**, 471 (1972).
- [38] P. Atten and J. C. Lacroix, Non-linear hydrodynamic stability of liquids subjected to unipolar injection, *J. de Méc.* **18**, 469 (1979).
- [39] K. P. Watson, Electrohydrodynamic stability of space-charge-limited currents in dielectric liquids. ii. Experimental study, *Phys. Fluids* **13**, 1955 (1970).
- [40] A. Castellanos, P. Atten, and A. T. Pérez, Finite amplitude electroconvection in liquids in the case of weak unipolar injection, *Physicochem. Hydrodynam.* **9**, 443 (1987).
- [41] J. C. Lacroix, P. Atten, and E. J. Hopfinger, Electro-convection in a dielectric liquid layer subjected to unipolar injection, *J. Fluid Mech.* **69**, 539 (1975).
- [42] P. Traoré and Jian Wu, On the limitation of imposed velocity field strategy for coulomb-driven electroconvection flow simulations, *J. Fluid Mech.* **727**, R3 (2013).
- [43] J. Wu, P. Traoré, P. A. Vázquez, and A. T. Pérez, Onset of convection in a finite two-dimensional container due to unipolar injection of ions, *Phys. Rev. E* **88**, 053018 (2013).
- [44] J. Wu, P. Traoré, and C. Louste, An efficient finite volume method for electric field-space charge coupled problems, *J. Electrostat.* **71**, 319 (2013).
- [45] P. Atten, D. Koulova-Nenova, and A. T. Pérez, On the EHD instability of a layer of insulating liquid subjected to a unipolar charge injection due to corona discharge in air, in *Proceedings of the International Workshop on Electrical Conduction, Convection and Breakdown in Fluids, Sevilla, 1998* (Universidad de Sevilla, Secretariado de Publicaciones, 1998), pp. 47–51.
- [46] F. Vega and A. T. Pérez, Instability in a non-ohmic/ohmic fluid interface under a perpendicular electric field and unipolar injection, *Phys. Fluids* **14**, 2738 (2002).
- [47] R. Chicón and A. T. Pérez, Instability of an interface between air and a low conducting liquid subjected to charge injection, *Phys. Fluids* **18**, 104108 (2006).
- [48] R. Chicón and A. T. Pérez, The stability of a horizontal interface between air and an insulating liquid subjected to charge injection, *Phys. Fluids* **26**, 034103 (2014).
- [49] H. G. Weller, G. Tabor, H. Jasak, and C. Fureby, A tensorial approach to computational continuum mechanics using object-oriented techniques, *Comput. Phys.* **12**, 620 (1998).
- [50] A. Castellanos and A. Gonzalez, Nonlinear electrohydrodynamics of free surfaces, *IEEE Trans. Dielectr. Electr. Insul.* **5**, 334 (1998).
- [51] J. R. Melcher, *Continuum Electromechanics*, Vol. 2 (MIT Press, Cambridge, MA, 1981).
- [52] A. Castellanos, *Electrohydrodynamics*, Vol. 380 (Springer Science & Business Media, New York, 1998).
- [53] C. W. Hirt and B. D. Nichols, Volume of fluid (VOF) method for the dynamics of free boundaries, *J. Comput. Phys.* **39**, 201 (1981).
- [54] I. Barton, Comparison of SIMPLE- and PISO-type algorithms for transient flows, *Int. J. Numer. Methods Fluids* **26**, 459 (1998).
- [55] F. Moukalled, L. Mangani, M. Darwish *et al.*, The finite volume method in computational fluid dynamics, in *An Advanced Introduction with OpenFoam and Matlab* (Springer, New York, 2016).
- [56] B. P. Leonard, A stable and accurate convective modelling procedure based on quadratic upstream interpolation, *Comput. Methods Appl. Mech. Eng.* **19**, 59 (1979).
- [57] B. Van Leer, Towards the ultimate conservative difference scheme, *J. Comput. Phys.* **135**, 229 (1997).
- [58] R. Deepak Selvakumar, J. Wu, J. Huang, and P. Traoré, Electrothermo-convection in a differentially heated square cavity under arbitrary unipolar injection of ions, *Int. J. Heat Fluid Flow* **89**, 108787 (2021).
- [59] M. Samir and P. Milovan, Computation of free surface flows using interface-tracking and interface-capturing methods, in *Nonlinear Water Wave Interaction* (WIT Press/Computational Mechanics Publications, Southampton, 1998).

- [60] O. Ubbink and R. I. Issa, A method for capturing sharp fluid interfaces on arbitrary meshes, *J. Comput. Phys.* **153**, 26 (1999).
- [61] X. Shan, Simulation of Rayleigh-Bénard convection using a lattice boltzmann method, *Phys. Rev. E* **55**, 2780 (1997).
- [62] K. Luo, J. Wu, Hong Liang Yi, and He Ping Tan, Three-dimensional finite amplitude electroconvection in dielectric liquids, *Phys. Fluids* **30**, 023602 (2018).
- [63] J. Wu, P. Traoré, A. T. Pérez, and Pedro A. Vázquez, On two-dimensional finite amplitude electro-convection in a dielectric liquid induced by a strong unipolar injection, *J. Electrostat.* **74**, 85 (2015).
- [64] R. Chicón, A. Castellanos, and E. Martin, Numerical modelling of Coulomb-driven convection in insulating liquids, *J. Fluid Mech.* **344**, 43 (2000).